

# Assessing the Accuracy of High-Resolution X-Ray Computed Tomography of Primate Trabecular Bone by Comparisons With Histological Sections

Roberto José Fajardo,<sup>1\*</sup> T.M. Ryan,<sup>2</sup> and J. Kappelman<sup>2</sup>

<sup>1</sup>*Interdepartmental Doctoral Program in Anthropological Sciences, State University of New York at Stony Brook, Stony Brook, New York 11794*

<sup>2</sup>*Department of Anthropology, University of Texas at Austin, Austin, Texas 78712*

**KEY WORDS** high-resolution X-ray computed tomography; primate trabecular bone; stereology; thresholding

**ABSTRACT** Different lines of evidence suggest that trabecular bone architecture contains a functional signal related to an organism's locomotor behavior. An understanding of the interspecific and intraspecific variation in extant nonhuman primate trabecular structure is needed to evaluate its usefulness as a tool to reconstruct the locomotor habits of extinct primates. High-resolution X-ray computed tomography (HRXCT) is a new imaging approach with a resolution in the tens of microns that allows nondestructive access to the internal structure of bony elements. Previous studies indicate that such resolution is necessary to accurately quantify structural parameters of trabecular bone.

The primary goal of this study was to test the accuracy of HRXCT by comparing stereological measurements from HRXCT images and histological thin sections of cancellous bone taken from the proximal femur and humerus of baboons. To this end, 11 bone samples were scanned on an HRXCT scanner and then thin-sectioned to reveal the scanned plane. HRXCT images were thresholded using a modified half-maximum height protocol. The stereological measurements included bone volume fraction (BV/TV), trabecular number (Tb.N), bone surface to volume ratio (BS/BV), trabecular thickness (Tb.Th), and trabecular

spacing (Tb.Sp). The measurement errors on the HRXCT images were 10.90% for BV/TV, 6.06% for Tb.N, 14.19% for BS/BV, 14.33% for Tb.Th, and 7.09% for Tb.Sp, but none of these measurements were significantly different from the histological standards ( $\alpha = 0.05$ ).

A second goal of this study was to examine the influence of thresholding, a necessary step in any morphometric study using computed tomography, on the accuracy of the quantitative morphometry. Threshold values derived from a modified half-maximum height protocol showed that parameters derived from the region of interest (area in which stereological measurements were later taken) produced better reconstructions of the actual bone structure than threshold values derived from more inclusive areas of bone.

We conclude that HRXCT can accurately reconstruct the complex architecture of trabecular bone, and that thresholding is a nontrivial step in trabecular bone studies, with even slight changes in the protocol greatly affecting the morphometric data. HRXCT represents a valuable analytical tool that should be of interest to a great many researchers in physical anthropology because it allows nondestructive access to internal morphology, thereby preserving valuable and limited skeletal collections. *Am J Phys Anthropol* 118:1–10, 2002. © 2002 Wiley-Liss, Inc.

Since the mid- to late-1800s, researchers have been investigating the architecture of cancellous bone and the nature of its correspondence to biomechanical loading. The growing theoretical, experimental, and comparative evidence suggests that cancellous bone reflects a history of loading (Kummer, 1959; Lanyon, 1974; Oxnard and Yang, 1981; Thomason, 1985; Heller, 1989; Goldstein et al., 1991; Rafferty and Ruff, 1994; Biewener et al., 1996; Rafferty, 1996, 1998; Galichon and Thackeray, 1997; Swartz et al., 1998; Fyhrie and Kimura, 1999; Macchiarelli et al., 1999; Rook et al., 1999; Huiskes, 2000; Huiskes et al., 2000), and it has been shown to alter in response to changes in, for example, gait (Pauwels, 1960).

Much of the previous work done on cancellous bone generally focused on three different visualization methods: histological thin sections, planar ra-

diography, and conventional computed tomography (CT). Histological methods, until very recently, were the only method that facilitated accurate morphometry of trabecular architecture (e.g., Merz and Schenk, 1970; Simon and Radin, 1972; Radin et al.,

Grant sponsor: NSF; Grant numbers: IIS-9816644, BCS9904925, BCS 9908847; Grant sponsor: L.S.B. Leakey Foundation.

\*Correspondence to: Roberto José Fajardo, Department of Anatomical Sciences, State University of New York at Stony Brook, Stony Brook, NY 11794-8081. E-mail: rfajardo@ic.sunysb.edu

Received 10 January 2001; accepted 21 December 2001.

Published online in Wiley InterScience (www.interscience.wiley.com).

DOI 10.1002/ajpa.10086

1973; Parfitt et al., 1983). Unfortunately, this method is destructive and, therefore, an unrealistic option for broad-scale intra- and interspecific studies of human or nonhuman primate bones (extant and fossil) housed in museum collections. Advances in X-ray imaging methods have helped researchers gain valuable insights into the structural organization and density of trabecular bone from different skeletal locations, without permanently damaging specimens (e.g., Kummer, 1959; Pauwels, 1960; Oxnard and Yang, 1981; Galichon and Thackeray, 1997; MacLatchy and Chen, 1997; Rafferty 1998; Marchiarelli et al., 1999). However, these methods are unable to further an appreciation of the structural morphometry of cancellous bone because they cannot produce images with sufficiently high resolution for the accurate measurement of variables such as the trabecular number or trabecular thickness.

Over the last decade or so, the intricate structure of cancellous bone has been studied using microcomputed tomography ( $\mu$ CT; Layton et al., 1988; Odgaard et al., 1990; Peyrin et al., 1993; Bonse et al., 1994; R uegsegger et al., 1996; Kapadia et al., 1998; Kinney et al., 1998). The numerous systems in use range in their nominal resolution capabilities between 2–100  $\mu$ m. In this paper, a new system for producing images of trabecular architecture is presented.

High-resolution X-ray computed tomography (HRXCT), like the microcomputed tomography ( $\mu$ CT) methods that already have been presented in the biomechanical and orthopaedic literature (Layton et al., 1988; Odgaard et al., 1990; Peyrin et al., 1993; Bonse et al., 1994; R uegsegger et al., 1996; Kapadia et al., 1998; Kinney et al., 1998), offers a new approach to studying trabecular architecture. Like conventional CT and  $\mu$ CT, HRXCT directs a plane of X-rays through an object. The intensity of the X-ray beam is measured before and after passing through the object, with the difference in X-ray attenuation representing the object's density. The object is rotated through 360° to complete the scan of a single slice. The intensity differences are converted to an image, with each pixel assigned a grayscale value that corresponds to the linear attenuation coefficient and the density at each point in the object. Additional slices through the object are taken to complete a three-dimensional (3-D) scan (for a review of CT technology, see Hendee, 1983).

HRXCT departs from conventional CT in its ability to achieve higher resolution, and from conventional CT and  $\mu$ CT in its ability to penetrate dense objects (Kappelman, 1998). HRXCT typically combines higher energy sources (200–400 kV) than those available in conventional CT and  $\mu$ CT, with modular linear and areal detector arrays. This combination produces a scanner capable of handling a variety of very dense samples across a wide range of resolutions. In comparison to conventional CT, HRXCT can produce images slices that range be-

tween 0.100–0.010 mm (Rowe et al., 1997), while conventional CT can produce image slices as thin as 0.500 mm. This point is important because comparative studies indicate that trabecular thicknesses are relatively invariant across mammal groups (Mullender et al., 1996; Swartz et al., 1998). Since trabecular thicknesses commonly range between 0.200–0.400 mm (Mullender et al., 1996), but might achieve thicknesses as high as 0.800 mm in some regions (Fajardo and M uller, 2001), the imaging limits of conventional CT could produce rather high errors in representation of the trabeculae (M uller et al., 1996; Kothari et al., 1998). Small specimens can be scanned nondestructively using both  $\mu$ CT and HRXCT (MacLatchy and M uller, 2000; Ryan, 2000, 2001). However, most  $\mu$ CT systems have small gantries that limit the size range of specimens that can be scanned (e.g., R uegsegger et al., 1996). The HRXCT used in this study system has a large specimen gantry that can hold objects 500 mm in diameter by 700 mm in length, which makes it possible to scan objects with a wide range of sizes nondestructively.

The purpose of this study was to assess the accuracy of HRXCT-based measurements of trabecular bone architecture when compared with those from traditional thin-sectioning techniques. Although 3-D reconstructions are possible using HRXCT, an evaluation of its accuracy is only possible in two dimensions due to the planar nature of histological samples. The HRXCT instrument used in this study is housed at the University of Texas at Austin (Bio-Imaging Research, Inc., Lincolnshire, IL; see <http://www.ctlab.geo.utexas.edu/>). There are other high-resolution CT scanners with similarly large gantries in use, especially in industry, but we are only aware of one that has been mentioned in biological research (Brochu, 1999).

The ability of the HRXCT scanner to scan objects of various sizes and to nondestructively access the internal morphology of bones has great potential for use by physical anthropologists across all subfields. It is anticipated that HRXCT will be of general interest to researchers in accurately measuring trabecular bone architecture because it allows for non-destructive analyses of bone structure using limited and irreplaceable skeletal collections.

## MATERIALS AND METHODS

### Specimen preparation and HRXCT scanning

Trabecular bone samples were taken from one humeral and one femoral head of seven adult *Papio cynocephalus* individuals housed in the osteology collection at the University of Texas at Austin and originally derived from the Southwest Foundation for Biomedical Research in San Antonio. As participants in dietary studies, the individuals were sacrificed at age 8.5 years, autopsied, and then skeletonized. None displayed any pathologic conditions, or had been used in disease-related research.

Two slices of trabecular bone of approximately 5–10 mm in thickness were extracted from each bone with a rotary saw, yielding a total of 28 trabecular bone samples. Both cut surfaces on each sample were ground smooth and parallel to each other, using a 40- $\mu\text{m}$  grit on a horizontal grinding wheel. Each sample was then scanned on the HRXCT scanner at the University of Texas at Austin. Four slices were scanned for each sample. Scans were collected beginning 1 mm from the cut and ground surface in order to avoid the bone dust produced by the sawing and grinding that accumulated within the marrow spaces. Scans were taken with a 40- $\mu\text{m}$  interslice spacing and 40- $\mu\text{m}$  slice thickness. The samples were scanned with a setting of 180 kV/0.133 mA source energy and 67-mm source-object distance. The images were reconstructed from 1,800 views and the field of view (FOV) was 34 mm, producing a pixel size of 33.20  $\mu\text{m}$ . All resulting images were eight-bit, with a potential range of 256 CT values.

After HRXCT scanning, the samples were soaked for 24 hr in 100% pure denatured ethyl alcohol and agitated in an ultrasonerator for about 5–10 min in order to dislodge as much residual bone dust and marrow as possible. Each sample was placed with the scanned side down (i.e., the side closest to the scan plane) in a flat-bottomed container. A 12% epoxy solution consisting of epoxy shell resin #815C and triethylenetetramine (TETA) hardener (E.V. Roberts, Culver City, CA) was used to embed each sample. Each epoxy-covered sample was vacuumed for about 5 min in order to fully impregnate the trabecular bone with epoxy, and the samples were allowed to cure overnight in an oven heated to between 80–100°F.

The next step in preparation was to produce standard histological thin sections of each sample. The embedded samples were removed from their containers and ground briefly on a horizontal diamond rotary lap grinder with a 20- $\mu\text{m}$  grit in order to expose the bone surface. Each sample was next trimmed about 1.5–1.75 mm from the scanned edge, using a low-speed metallurgical diamond wheel saw, and then ground to a 1-mm thickness, using a horizontal diamond rotary lap grinder with a 40- $\mu\text{m}$  grit. The cut surface was ground as close as possible to the 1-mm plane that had been HRXCT-scanned. The ground surface was fixed to a glass slide using Loctite ultraviolet-curing epoxy and ground to <100  $\mu\text{m}$ , using a Hillcrest thin-section machine. Samples were cleaned with isopropyl alcohol and allowed to air dry. All prepared thin sections and a millimeter scale bar, for measurement calibration, were then digitized, using a Nikon LS-3510AF slide scanner. Pixel size for the scanned thin sections was 17.24  $\mu\text{m}$ .

#### Region of interest selection

One potential source of error in this study was the inability to match the HRXCT scanned plane with the histological thin-sectioned plane. Since the goal was to test the accuracy of the HRXCT scanner,

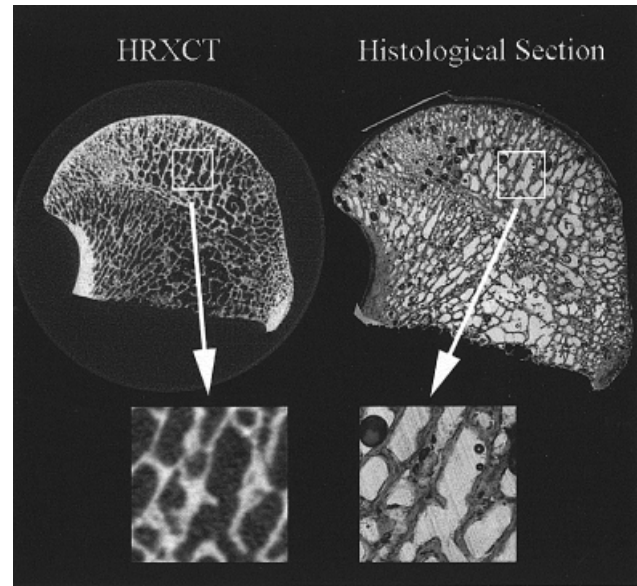


**Fig. 1.** Regions of interest (ROI, 4  $\times$  4 mm) for structural analysis were selected from each HRXCT and thin-section image.

some discrimination of the full data set was necessary. Some samples were excluded for reasons such as incomplete infiltration by the epoxy or poor trabecular structure (i.e., very little trabecular bone). The best matches between an HRXCT image slice and a histological section were determined by evaluating the presence of easily identified bone markers. These markers were in the form of terminal trabeculae or irregular shapes that facilitated matching the two planes. After visual inspection, 11 pairs of histological and HRXCT slices remained for analysis. Quantitative histomorphometric analyses of the HRXCT and histological section pairs were conducted on a square region of interest (ROI) with an edge length of 4 mm (Fig. 1). Care was taken to ensure that each ROI consisted entirely of trabecular bone. Image analyses were conducted on a Macintosh PowerPC computer, using the public domain NIH Image software (PPC version 1.61, developed at the U.S. National Institutes of Health, and available at <http://rsb.info.nih.gov/nih-image/>).

#### HRXCT image thresholding

In order to collect trabecular bone morphometric data from HRXCT scans, it is first necessary to threshold or segment the HRXCT images. In this study, image segmentation refers to the process of separating the bone phase from the nonbone phase in the image, as determined from pixel grayscale values. In HRXCT data, each grayscale value corresponds to a material density, and a specific threshold value that best separates bone from air must be chosen. The selection of this threshold value is critical to producing an accurate representation of the bone because the bone-nonbone boundary is represented by a gradient of gray values rather than a discrete interface. An over- or underestimation of

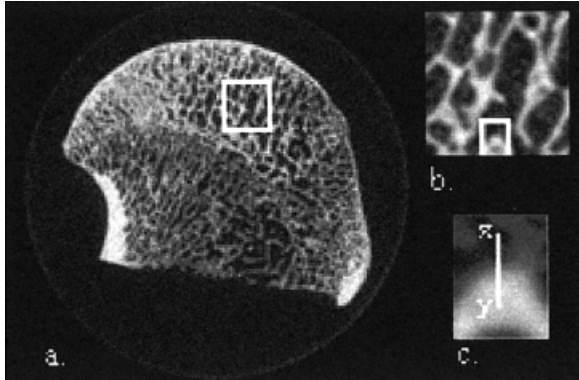


**Fig. 2.** Threshold in the ROI-Tb image set was determined by sampling 10 bone-nonbone boundaries in ROI (b) of the complete HRXCT image (a). Steps in this process are as follows. First, an ROI is selected from the larger image. Next, grayscale values are sampled across the boundary of a bone-nonbone interface (c) to determine half-maximum height (HMH), which is the average of maximum and minimum grayscale values. This step is repeated 10 times in an ROI, and the mean HMH is determined.

the threshold value will affect the position of the bone's actual boundaries and, consequently, the accuracy of any area or linear measurements (Spoor et al., 1993).

Spoor et al. (1993) presented a threshold protocol called the half-maximum height (HMH). This approach defines the specific bone-nonbone boundary as the midpoint between the first maximum and minimum gray values along a row of pixels that span the bone-nonbone transition. This approach works well with linear measurements on bone shafts and enamel thicknesses, where specific planes or dimensions are of interest (Spoor et al., 1993; Corcoran et al., 1994). However, in stereological studies of cancellous bone, trabeculae are not individually measured. Instead, the structure is characterized through the superposition of points or a grid on an area of cancellous bone and by analyzing the intersection of the trabeculae and the test grid. Therefore, a segmentation protocol that applies a different threshold to each bone-nonbone boundary for every trabecular strut in an image is not practical.

Since the HMH thresholding technique does approximate the bone boundary in a CT image, this approach was modified to facilitate the goal of quantifying the trabecular architecture in HRXCT images and comparing these results with those obtained from histological sections. In each  $4 \times 4$  mm ROI, 10 trabecular bone-nonbone boundaries were selected at random (Fig. 2). Then, the HMH was calculated for a row of pixels across each bone-nonbone interface for all 10 sampling sites. The mean HMH for all 10 sites was used as that image's threshold level (ROI-Tb protocol).

Since each image's specific threshold was a function of bone-nonbone sampling, it is reasonable to expect that the threshold value could change depending on the locations that were sampled in each image. For example, cortical bone has a greater min-

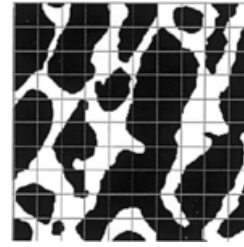


**Fig. 3.** Stereological grid superimposed on a thresholded HRXCT image. Intersections of lines are used as points for determination of bone volume fraction ( $P_V$ ). The path of grid lines and their relationship to bone boundaries (intersections of bone and grid lines) are used to calculate the trabecular number ( $P_L$ ).

eral density (Gong *et al.*, 1964; Currey, 1988) and much lower porosity than cancellous bone, which should result in higher HMH values. To examine the effect of sampling, two additional image sets were created, using the original scan data but slightly different threshold protocols. In the first set, five cortical bone-nonbone and five trabecular bone-nonbone boundaries were sampled in each HRXCT image (hereafter referred to as Co-Tb). The cortical bone samples were taken from random sites in each full image and included regions of the humeral and femoral necks and the subchondral cortical bone. The five trabecular bone boundary samples were also chosen at random from within the entire marrow cavity, and not restricted to the region of interest. In the second set of images, 10 boundaries of trabecular bone were sampled. These trabeculae samples were taken from across the entire marrow cavity as well (referred to as Full-Tb), and were not restricted to the  $4 \times 4$  mm area as in the ROI-Tb protocol. Kolmogorov-Smirnov one-sample tests for normality indicated that the HMH data were normally distributed. Consequently, paired-sample *t*-tests were used to determine whether there were any significant differences ( $\alpha = 0.05$ ) in the threshold values produced by the three different threshold protocols.

### Stereological analysis

Stereological analyses rely on the superposition of grids on two-dimensional images (Fig. 3). Two fundamental counts are made from the superposition of this grid on the trabecular bone image: 1)  $P_V$ , or the ratio of grid points lying in the bone phase to the total number of grid points; and 2)  $P_L$ , or the number of intersections between the bone and test lines in the grid per unit test-line length (Underwood, 1970; Feldkamp et al., 1989; Howard and Reed, 1998). The NIH Image Cavalieri macro was used to superimpose grids with a  $400\text{-}\mu\text{m}$  spacing on histological and HRXCT images. This grid spacing produced lines that were 12 pixels apart in the HRXCT images (1 pixel =  $33.20\ \mu\text{m}$ ) and 23 pixels apart (1 pixel =  $17.24\ \mu\text{m}$ ) in the histological images. A point was counted as lying within bone only when it was completely surrounded by white pixels. An average  $P_L$

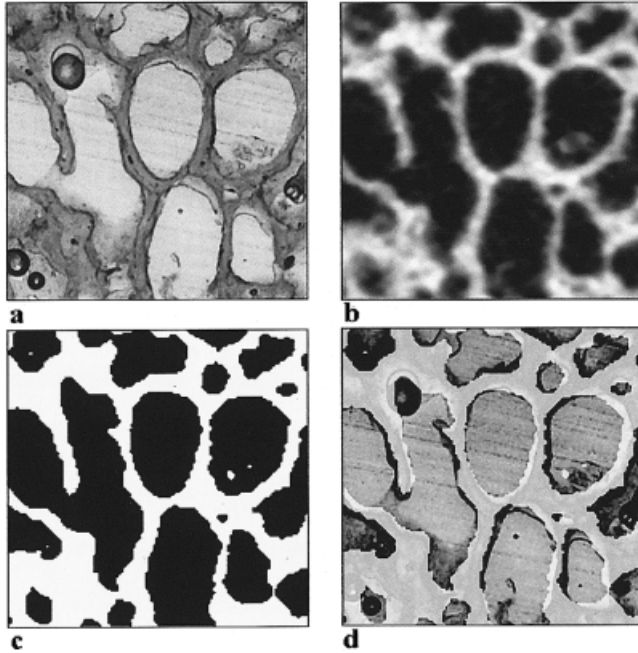


**Fig. 4.** Four comparisons of trabecular bone architecture in corresponding histological and HRXCT images. **a:** Histological-section ROI. **b:** Corresponding HRXCT ROI. **c:** HRXCT image after thresholding. **d:** Composite of thresholded HRXCT image (represented in white, but with opacity reduced so that both structures can be seen) and the histological section. Trabeculae in the HRXCT image are sometimes thicker than corresponding trabeculae in the histological image, and can be seen as white edges in this composite image.

was calculated from two perpendicular grids (Parfitt et al., 1983). From manual counts of  $P_P$  and  $P_L$ , morphometric parameters of trabecular architecture were derived, using the plate model of Parfitt et al. (1983). These structural measurements and their derivation from  $P_P$  and  $P_L$  counts are listed below.

$$\text{Trabecular bone volume fraction (BV/TV)} \\ = P_P (\%) \quad (1)$$

$$\text{Mean trabecular plate number (Tb.N)} \\ = P_L (\text{mm}^{-1}) \quad (2)$$

$$\text{Bone surface to volume ratio (BS/BV)} \\ = 2P_L/P_P (\text{mm}^2/\text{mm}^3) \quad (3)$$

$$\text{Mean trabecular plate thickness (Tb.Th)} \\ = P_P/P_L (\text{mm}) \quad (4)$$

$$\text{Mean trabecular plate separation (Tb.Sp)} \\ = (1 - P_P)/P_L (\text{mm}) \quad (5)$$

The specific surface, or BS/BV, is a measure of the surface area per unit trabecular bone volume (Merz and Schenk, 1970). This measurement helps to characterize the diameters of trabeculae within a volume. A high BS/BV value indicates that trabecular cross sections are small, while a low value indicates a higher strut diameter.

**TABLE 1.** Results of repeated measurements on one image thresholded by sampling trabecular bone-nonbone boundaries within region of interest (ROI-Tb) and one histological section<sup>1</sup>

Trial	HRXCT scan		Histological section	
	$P_P$ (%)	$P_L$ ( $\text{mm}^{-1}$ )	$P_P$ (%)	$P_L$ ( $\text{mm}^{-1}$ )
1	33.0	1.80	32.0	1.59
2	33.0	1.80	30.0	1.61
3	33.0	1.80	32.0	1.56
4	33.0	1.81	33.0	1.53
5	33.0	1.81	31.0	1.57
6	33.0	1.80	31.0	1.59
Mean	33.0	1.80	31.5	1.58
SD	0.0	0.01	1.0	0.03
CV	0.0	0.32	3.3	1.69

<sup>1</sup>  $P_P$ , ratio of grid points lying in bone phase to total number of grid points;  $P_L$ , number of intersections between bone and superimposed test lines per unit test line length.

All structural parameters were measured on the histological samples and each of the three HRXCT threshold image sets, ROI-Tb, Co-Tb, and Full-Tb. Means and standard deviations were calculated for all image sets. In addition, the mean actual and mean percent differences between the measurements made on the histological sections and the HRXCT image sets were calculated. The percent difference provides a measure of the discrepancy between the two measurements and uses the histological value as the standard. It is defined here as the difference between the histological and HRXCT values divided by the value taken from the histological section ( $[\text{histology value} - \text{HRXCT value}/\text{histology value}] * 100 = \text{percentage difference}$ ). A negative value indicates that the HRXCT-based value overestimates the histological standard. Kolmogorov-Smirnov one-sample tests for normality indicated that the stereological measurement data were normally distributed. Consequently, paired-samples  $t$ -tests were used to test the hypothesis that there were no significant differences between histological and HRXCT measurements. Measurements were repeated six times on one histological sample and one HRXCT sample in order to test the precision (reproducibility) of the results.

## RESULTS

The high degree of similarity in trabecular bone architecture seen in the HRXCT scans and the histological sections is illustrated in Figure 4. The top row of Figure 4 shows the corresponding region of trabecular bone from a thin section and from an HRXCT scan, while the bottom row shows the ROI-Tb thresholded image and a composite of that image with the histological section. The high degree of congruence of the two image-acquisition techniques is apparent.

Repeated measurements on one histological section and one thresholded HRXCT image demonstrated that the stereological measuring protocol was reliable (Table 1). The individual counts made on the thresholded HRXCT image approximated each other quite closely, due to the distinct boundary

TABLE 2. Results of stereological analysis on histological thin sections and ROI-Tb images<sup>1</sup>

	Specimen											Mean ( $\pm$ SD)
	1	2	3	4	5	6	7	8	9	10	11	
BV/TV (%)												
Histology	42.0	30.0	35.0	41.0	31.0	33.0	47.0	46.0	25.0	16.0	28.0	34.0 ( $\pm$ 9.5)
ROI-Tb	42.0	30.0	32.0	33.0	31.0	26.0	42.0	49.0	30.0	19.0	32.0	33.3 ( $\pm$ 8.3)
Tb.N ( $\text{mm}^{-1}$ )												
Histology	1.65	1.44	1.84	1.84	2.05	1.78	2.08	2.22	2.32	1.70	1.56	1.86 ( $\pm$ 0.28)
ROI-Tb	1.65	1.41	1.73	1.82	2.07	2.05	1.92	1.83	2.14	1.59	1.59	1.80 ( $\pm$ 0.23)
BS/BV ( $\text{mm}^2/\text{mm}^3$ )												
Histology	7.86	9.60	10.51	8.98	13.23	10.79	8.85	9.65	18.56	21.25	11.14	11.86 ( $\pm$ 4.26)
ROI-Tb	7.86	9.40	10.81	11.03	13.35	15.77	9.14	7.47	14.27	16.74	9.94	11.43 ( $\pm$ 3.15)
Tb.Th (mm)												
Histology	0.255	0.208	0.190	0.223	0.151	0.185	0.226	0.207	0.108	0.094	0.179	0.184 ( $\pm$ 0.049)
ROI-Tb	0.255	0.213	0.185	0.181	0.150	0.127	0.219	0.268	0.140	0.119	0.201	0.187 ( $\pm$ 0.050)
Tb.Sp (mm)												
Histology	0.352	0.486	0.353	0.321	0.337	0.376	0.255	0.243	0.323	0.494	0.462	0.364 ( $\pm$ 0.085)
ROI-Tb	0.352	0.496	0.393	0.368	0.333	0.361	0.302	0.279	0.327	0.509	0.428	0.377 ( $\pm$ 0.074)

<sup>1</sup> BV/TV, bone volume fraction; Tb.N, average trabecular number; BS/BV, bone surface to bone volume ratio; Tb.Th, average trabecular thickness; Tb.Sp, average trabecular separation; ROI-Tb, region of interest threshold protocol (see Methods for protocol definition).

TABLE 3. Mean actual and mean percent error ( $\pm$  SD) between stereological parameters calculated on histological thin sections and ROI-Tb images<sup>1</sup>

BV/TV		
Actual		3.5 ( $\pm$ 2.7)
Percent		10.9 ( $\pm$ 8.5)
Tb.N		
Actual		0.12 ( $\pm$ 0.12)
Percent		6.06 ( $\pm$ 5.84)
BS/BV		
Actual		1.83 ( $\pm$ 1.93)
Percent		14.19 ( $\pm$ 14.43)
Tb.Th		
Actual		0.02 ( $\pm$ 0.02)
Percent		14.33 ( $\pm$ 13.20)
Tb.Sp		
Actual		0.02 ( $\pm$ 0.02)
Percent		7.09 ( $\pm$ 6.61)

<sup>1</sup> Abbreviations: see Tables 1 and 2.

created between bone and nonbone in the segmentation process. The histological results were not as consistent as the HRXCT because of errors associated with determining the exact position of the bone-nonbone boundaries on these images. The results of this precision test clearly demonstrated the replicability of stereological measurements.

In general, the mean values calculated from the ROI-Tb images corresponded to the same set of measurements taken on the histological samples (Table 2). Errors ranged between 6% and approximately 14% for the primary and derived structural variables, but the statistical tests indicated that none of the ROI-Tb measurements were significantly different from the same measurements made on histological thin sections (Tables 3 and 4).

The relative error, which takes into account the sign of the error value, helps to understand whether measurements on ROI-Tb images tend to be overestimated or underestimated compared to the histological standard. The relative percentage error for BV/TV was 0.03%, and 2.78% for Tb.N (Table 5). This means that these measurements tended to be

slightly underestimated in the ROI-Tb images. BS/BV also tended to be underestimated, while the negative values for Tb.Th and Tb.Sp indicated that these variables were overestimated in comparison to the histological thin sections.

The results of this study provide clear evidence that different segmentation protocols can impact the threshold applied and the subsequent morphometric measurements. The mean HMH value for the ROI-Tb protocol was 132.85, 134.69 for the Co-Tb protocol, and 143.40 for the Full-Tb protocol. The HMH values determined by the Full-Tb approach were significantly different ( $\alpha = 0.05$ ) from the HMH values determined by the other two protocols (Table 6). However, no significant differences were found between threshold values for Co-Tb and ROI-Tb protocols.

Even though the thresholds applied to the Co-Tb set of images were not found to be significantly different from the ROI-Tb set, the structural measurements taken on the Co-Tb image set did not correspond to the measurements from the histological sections as well (Tables 7 and 8). The mean percentage errors in Co-Tb measurements exceeded the error found in the ROI-Tb images in all variables except BS/BV. Two of these Co-Tb measurements, Tb.N and Tb.Sp, were significantly different from the same measurements made on the thin sections (see Table 4). The greatest measurement errors, which reached 32.74% for Tb.N, were produced by the Full-Tb thresholding in all but one instance (Tables 7 and 8). Tb.Sp showed only 7.93% error, which was the closest correspondence to the histological sections of all Tb.Sp counts and was the only Full-Tb measurement that was not significantly different from the standard (see Table 4).

The trends in the Co-Tb and Full-Tb data were rather similar (Table 8). Relative percentage error data indicated that both image sets tended to underestimate Tb.N and BS/BV, and overestimate Tb.Th and Tb.Sp. BV/TV, on the other hand, was underes-

TABLE 4. Results of paired *t*-tests for each stereological parameter

	ROI-Tb		Co-Tb		Full-Tb	
	<i>t</i>	<i>P</i>	<i>t</i>	<i>P</i>	<i>t</i>	<i>P</i>
BV/TV	0.539 <sup>n.s.</sup>	0.602	0.209 <sup>n.s.</sup>	0.839	-4.94*	0.001
Tb.N	1.25 <sup>n.s.</sup>	0.239	3.03*	0.013	2.26*	0.047
BS/BV	0.52 <sup>n.s.</sup>	0.614	0.856 <sup>n.s.</sup>	0.412	3.41*	0.007
Tb.Th	-0.291 <sup>n.s.</sup>	0.777	-1.18 <sup>n.s.</sup>	0.266	-3.70*	0.004
Tb.Sp	-1.65 <sup>n.s.</sup>	0.130	-2.25*	0.048	-0.254 <sup>n.s.</sup>	0.805

\* Significant at  $\alpha = 0.05$ ; n.s., not significant. Co-Tb, image sample thresholded using cortical and trabecular bone boundaries in modified HMH protocol; Full-Tb, image set thresholded using trabecular bone boundaries from an entire image (beyond region of interest) in modified HMH protocol; for other abbreviations, see Tables 1 and 2.

TABLE 5. Mean relative percent error ( $\pm$  SD) between measurements made on histological standards and ROI-Tb images<sup>1</sup>

BV/TV	0.03 ( $\pm$ 14.20)
Tb.N	2.78 ( $\pm$ 8.13)
BS/BV	0.34 ( $\pm$ 20.72)
Tb.Th	-3.95 ( $\pm$ 19.57)
Tb.Sp	-4.84 ( $\pm$ 8.56)

<sup>1</sup> Abbreviations: see Tables 1 and 2.

TABLE 6. Descriptive statistics for each mean half-maximum height (HMH) calculation and results of paired-samples tests

	Co-Tb	Full-Tb	ROI-Tb
Mean	134.69	143.40	132.85
SD	14.47	14.81	18.30
SE	1.38	1.41	1.74
	Co-Tb/Full-Tb	Co-Tb/ROI-Tb	Full-Tb/ROI-Tb
<i>t</i>	-4.32*	0.971 <sup>n.s.</sup>	5.37*
<i>p</i>	0.000	0.334	0.000

\* Significant at  $\alpha = 0.05$ ; n.s., not significant. SD, standard deviation of the mean, SE, standard error of the mean; for other abbreviations see Tables 1, 2, and 4.

TABLE 7. Results of stereological analysis on Co-Tb and Full-Tb images<sup>1</sup>

BV/TV (%)	
Co-Tb	33.6 ( $\pm$ 12.3)
Full-Tb	39.1 ( $\pm$ 10.5)
Tb.N (mm <sup>-1</sup> )	
Co-Tb	1.69 ( $\pm$ 0.23)
Full-Tb	1.69 ( $\pm$ 0.26)
BS/BV (mm <sup>2</sup> /mm <sup>3</sup> )	
Co-Tb	11.40 ( $\pm$ 4.61)
Full-Tb	9.34 ( $\pm$ 3.21)
Tb.Th (mm)	
Co-Tb	0.201 ( $\pm$ 0.076)
Full-Tb	0.238 ( $\pm$ 0.079)
Tb.Sp (mm)	
Co-Tb	0.398 ( $\pm$ 0.094)
Full-Tb	0.366 ( $\pm$ 0.076)

<sup>1</sup> mean ( $\pm$  SD). See Tables 2 and 4 for explanations of abbreviations. Co-Tb protocol includes regions of the humeral and femoral necks and the subchondral bone. Full-Tb protocol includes regions across the entire marrow cavity (see Materials and Methods for exact protocol definitions).

timated by Co-Tb images but overestimated by Full-Tb images.

## DISCUSSION

The primary objective of this study was to assess the accuracy of HRXCT images of trabecular bone

TABLE 8. Mean actual error, mean percentage error, and mean relative percentage error ( $\pm$  SD) between stereological parameters calculated on Co-Tb and Full-Tb images and histological sections<sup>1</sup>

	Co-Tb	Full-Tb
BV/TV		
Actual	3.8 ( $\pm$ 4.2)	5.3 ( $\pm$ 3.1)
Abs. Percent	11.1 ( $\pm$ 10.8)	16.8 ( $\pm$ 11.9)
Rel. Percent	1.8 ( $\pm$ 15.8)	-16.3 ( $\pm$ 12.7)
Tb.N		
Actual	0.17 ( $\pm$ 0.18)	0.23 ( $\pm$ 0.19)
Abs. Percent	8.58 ( $\pm$ 8.48)	11.94 ( $\pm$ 8.96)
Rel. Percent	8.40 ( $\pm$ 8.67)	8.55 ( $\pm$ 12.52)
BS/BV		
Actual	1.38 ( $\pm$ 1.14)	2.90 ( $\pm$ 1.94)
Abs. Percent	12.41 ( $\pm$ 11.74)	23.65 ( $\pm$ 10.67)
Rel. Percent	4.43 ( $\pm$ 16.90)	20.14 ( $\pm$ 16.83)
Tb.Th		
Actual	0.03 ( $\pm$ 0.04)	0.06 ( $\pm$ 0.04)
Abs. Percent	15.21 ( $\pm$ 19.27)	32.74 ( $\pm$ 20.00)
Rel. Percent	-8.29 ( $\pm$ 23.46)	-29.79 ( $\pm$ 24.55)
Tb.Sp		
Actual	0.04 ( $\pm$ 0.05)	0.03 ( $\pm$ 0.02)
Abs. Percent	11.22 ( $\pm$ 12.53)	7.93 ( $\pm$ 5.44)
Rel. Percent	-10.03 ( $\pm$ 13.59)	-1.71 ( $\pm$ 9.77)

<sup>1</sup> Abbreviations: see TABLES 2, 4, and 7. Abs., absolute; Rel., relative.

against those of traditional histological sections. Comparisons of stereological measurements taken from HRXCT scans thresholded using the bone boundaries within the region of interest with those taken on histological sections show that the HRXCT scanner used in this study is capable of accurately resolving nonhuman primate trabecular bone architecture.

The bone volume fraction and average trabecular number measurements provide two good tests of the accuracy of HRXCT imaging. These are the only two variables that are independently measured (i.e., not calculated from other variables), and each variable measures a different aspect of the trabecular bone structure. Of these two measurements, trabecular bone volume fraction (BV/TV), which is dependent on the amount of material present in an image and not its arrangement, offers what is probably a less precise test. The measurement of mean trabecular plate number (Tb.N) offers a more rigorous test of the scanner's accuracy because it is dependent on both the amount of bone and the arrangement of that bone in an image. The reason for this difference is that Tb.N is measured through counts of intersec-

tions of a grid of lines with bone in the image. If bony struts or marrow cavities disappear due to either the size or density of trabeculae or the thresholding technique, then Tb.N will be adversely affected. The results for the BV/TV and Tb.N parameters demonstrate that the images thresholded by analyzing specific bone-nonbone interfaces within the ROI accurately represent the amount and the arrangement of bone material.

The second objective of this study was to examine how changes in segmentation protocol affect threshold values and subsequent stereological analyses. Thresholds were based on an average HMH for each image, using three different sampling procedures. The statistical tests indicated that there was no difference in thresholds determined by the ROI-Tb and Co-Tb protocols (see Materials and Methods for protocol definitions). However, the actual differences in ROI-Tb and Co-Tb thresholds were sufficient to produce quite different results in the morphometric analyses. The importance of image thresholding is underscored by the fact that two Co-Tb structural parameters were significantly different from the histological standard, while the ROI-Tb measurements were not. In addition, these results demonstrate the importance of sampling the appropriate region and type of bone in order to determine accurate threshold values. Threshold values derived from bone types and regions outside the ROI may produce erroneous results due to variation in bone density.

One interesting result of this study is the observation that Tb.N was underestimated in every HRXCT image set relative to the histological sections. This underestimation of mean trabecular plate number can be attributed to two general causes. The first involves the interaction of voxel size and size of the trabeculae. When the trabeculae are small or thin relative to the volume of the voxel, this can cause an artifact called partial volume averaging. Since the density within any voxel is averaged over the densities of all objects within it, a very thin trabecula will be represented in an image by a lower CT number than the actual bone density of that trabecula, due to the presence of air or soft tissue (marrow) occupying most of the voxel. As a result, when images are thresholded, these thin trabeculae are lost because their CT values are artificially decreased and fall below the threshold set by HMH sampling bone-nonbone boundaries. A second possible (though unlikely) explanation is that the mineral density of bone in our sample was actually poor due to bone disorders such as osteopenia or osteoporosis, which appear to occur in primates (DeRousseau, 1985; Pope et al., 1989; Cahoon et al., 1996; Champ et al., 1996; Cerroni et al., 2000). While the sample did not show any obvious signs of bone disease (see Materials and Methods) and were rather young at death, the occurrence of either of these disorders in this sample cannot be fully discounted. In any case, either of these bone disorders

can affect the bone mineral density (i.e., can cause decreased mineral density) and porosity. If the adverse effects of osteopenia and osteoporosis are not distributed evenly across any area of trabecular bone, then this would result in a mosaic of CT values (and grayscale values) in a scanned sample. If the lower CT values in the range are lower than that of the threshold level, this low-density bone would disappear after thresholding is applied to the image, thus reducing the Tb.N. Although a series of different thresholds was applied to the images, each threshold gray value was determined with a relatively similar protocol by sampling HMH values. The ROI-Tb results were robust, but further study is required to determine exactly how different threshold approaches and scan parameters affect Tb.N counts.

A possible source of error throughout this study and any similar type of validation study is the difficulty in aligning the histological cut and the 40- $\mu$ m HRXCT scan planes. The results showed that this was not a large problem in this study, because the ROI-Tb image set produced similar measurements to those of thin sections, but it may have contributed to some of the large individual error, which reached as high as 27% (see Table 2, specimen 6 BV/TV) in the calculation of the primary variables. Any validation study of this type tests not only the accuracy of the imaging machinery and the quality of the image processing but also the ability of the researchers to match CT scan and histological cut planes. The results might have been better on an individual level had the HRXCT scan and thin-section planes been taken from each specimen's initial cut surface rather than from a plane 1 mm deep to the initial cut surface, but such an approach would not really have tested the scanner's ability to image the internal structure of bone.

The results of this accuracy study, along with two previous tests of the  $\mu$ CT method (Kuhn et al., 1990; Müller et al., 1998), demonstrate that HRXCT scanning is capable of producing images that closely correspond with histological sections. It is, of course, clear that the accuracy of any measurement of trabecular architecture is dependent on the resolution of the scan (Kuhn et al., 1990; Müller et al., 1996, 1998; Kothari et al., 1998), as well as on the segmentation protocol that is applied to the image. In this study, mean trabecular plate thickness showed the greatest percentage error in the ROI-Tb images, but the actual error of 0.02 mm was less than the size of one pixel. To achieve a better result, the scanner's settings would have to be set to a higher in-plane resolution (all else being equal).

In summary, this study demonstrates that HRXCT can be used to quantify the architecture of primate trabecular bone in a nondestructive manner. It is likely that future studies will offer new insights into the relationship between trabecular bone architecture and locomotor behavior in extant primates. Given the higher energy levels that are

found in HRXCT scanners, it is also likely that this technique can be used to image trabecular bone in fossil primates (Ryan, 2001), but positive results from these scans will of course be heavily dependent on the degree and pattern of mineralization of the specific fossil. Combining 3-D morphometric data that document extant primate trabecular architecture (Fajardo et al., 2000; MacLatchy and Müller, 2000; Ryan, 2000, 2001; Fajardo and Müller, 2001) and data from fossil primates is likely to provide new insights into the locomotor behaviors of living primates and offer a new method for reconstructing and testing the locomotor patterns of extinct species.

### ACKNOWLEDGMENTS

The authors thank Greg Thompson, Department of Geological Sciences Thin Section Laboratory at the University of Texas at Austin, for access to equipment, supplies, laboratory space, and thin-section knowledge; Claud Bramblett, Department of Anthropology at the University of Texas at Austin, for access to the *Papio* skeletal sample; and Richard Ketcham and Matthew Colbert for their help in HRXCT scanning. In addition, we thank Brigitte Demes and Jack Stern, whose comments on earlier drafts improved this manuscript greatly. This study and further studies of primate trabecular bone are funded in part by NSF IIS-9816644 (to J.K.), NSF BCS9904925 (to R.J.F.), and NSF BCS 9908847 (to T.M.R.), and by grants from the L.S.B. Leakey Foundation (to R.J.F. and T.M.R.).

### LITERATURE CITED

- Biewener AA, Fazzalari NL, Konieczynski DD, Baudinette RV. 1996. Adaptive changes in trabecular architecture in relation to functional strain patterns and disuse. *Bone* 19:1–8.
- Bonse U, Busch F, Gunnewig O, Beckmann F, Pahl R, Delling G, Hahn M, Graeff W. 1994. 3D computed X-ray tomography of human cancellous bone at 8  $\mu\text{m}$  spatial and  $10^{-4}$  energy resolution. *Bone Miner* 25:25–38.
- Brochu CA. 1999. High-resolution CT analysis of a *Tyrannosaurus rex* skull. *J Vert Paleontol* [Suppl] 19:34.
- Cahoon S, Boden SD, Gould KG, Vailas AC. 1996. Noninvasive markers of bone metabolism in the rhesus monkey: normal effects of age and gender. *J Med Primatol* 25:333–338.
- Cerroni AM, Tomlinson GA, Turnquist JE, Grynpsas MD. 2000. Bone mineral density, osteopenia, and osteoporosis in the rhesus macaques of Cayo Santiago. *Am J Phys Anthropol* 113:389–410.
- Champ JE, Binkley N, Havighurst T, Colman RJ, Kemnitz JW, Roecker EB. 1996. The effects of advancing age on bone mineral content of female rhesus monkeys. *Bone* 5:485–492.
- Corcoran TA, Sandler RB, Myers ER, Lebowitz HH, Hayes WC. 1994. Calculation of cross-sectional geometry of bone from CT images with application in postmenopausal women. *J Comput Assist Tomogr* 18:626–633.
- Currey JD. 1988. The effects of porosity and mineral content on the Young's modulus of elasticity of compact bone. *J Biomech* 21:131–139.
- DeRousseau CJ. 1985. Aging in the musculoskeletal system of rhesus monkeys: III. Bone loss. *Am J Phys Anthropol* 68:157–167.
- Fajardo RJ, Müller R. 2001. Three-dimensional analysis of non-human primate trabecular architecture using microcomputed tomography. *Am J Phys Anthropol* 115:327–336.
- Fajardo RJ, MacLatchy LM, Müller R. 2000. Analysis of femoral head trabecular architecture using  $\mu\text{CT}$ : evidence from some anthropoids and lorisoids. *Am J Phys Anthropol* [Suppl] 30:147.
- Feldkamp LA, Goldstein SA, Parfitt AM, Jesion G, Kleerekoper M. 1989. The direct examination of three-dimensional bone architecture in vitro by computed tomography. *J Bone Miner Res* 4:3–11.
- Fyhrie DP, Kimura JH. 1999. Cancellous bone biomechanics. *J Biomech* 32:1139–1148.
- Galichon V, Thackeray JF. 1997. CT scans of trabecular bone structure in the ilia of Sts 14 (*Australopithecus africanus*), *Homo sapiens* and *Pan paniscus*. *S Afr J Sci* 93:179–180.
- Goldstein SA, Matthews LS, Kuhn JL, Hollister SJ. 1991. Trabecular bone remodeling: an experimental model. *J Biomech* 24:135–150.
- Gong JK, Arnold JS, Cohn SH. 1964. Composition of trabecular and cortical bone. *Anat Rec* 149:325–331.
- Heller JA. 1989. Stress trajectories in the proximal femur of archaic *Homo sapiens* and modern humans. *Am J Phys Anthropol* [Suppl] 78:239.
- Hendee WR. 1983. Physical principles of computed tomography. Boston: Little, Brown & Co.
- Howard V, Reed M. 1998. Unbiased stereology: three-dimensional measurements in microscopy. New York: Springer.
- Huiskes R. 2000. If bone is the answer, then what is the question? *J Anat* 197:145–156.
- Huiskes R, Ruimerman R, van Lenthe GH, Janssen JD. 2000. Effects of mechanical forces on maintenance and adaptation of form in trabecular bone. *Nature* 405:704–706.
- Kapadia RD, Stroup GB, Badger AM, Koller B, Levin JM, Coatsney RW, Dodds RA, Liang X, Lark MW, Gowen M. 1998. Applications of micro-CT and MR microscopy to study pre-clinical models of osteoporosis and osteoarthritis. *Technol Health Care* 6:361–372.
- Kappelman J. 1998. Advances in three-dimensional data acquisition and analysis. In: Rosenberger A, Fleagle JG, McHenry M, Strasser E, editors. Primate locomotion. New York: Plenum. p 205–222.
- Kinney JH, Ryaby JT, Haupt DL, Lane NE. 1998. Three-dimensional *in vivo* morphometry of trabecular bone in the OVX rat model of osteoporosis. *Technol Health Care* 6:339–350.
- Kothari M, Keaveny TM, Lin JC, Newitt DC, Genant HK, Majumdar S. 1998. Impact of spatial resolution on the prediction of trabecular architecture parameters. *Bone* 22:437–443.
- Kuhn JL, Goldstein SA, Feldkamp LA, Goulet RW, Jesion G. 1990. Evaluation of a microcomputed tomography system to study trabecular bone structure. *J Orthop Res* 8:833–842.
- Kummer B. 1959. Bauprinzipien des Säugerskeletes. Stuttgart: Georg Thieme Verlag.
- Lanyon LE. 1974. Experimental support for the trajectorial theory of bone structure. *J Bone Joint Surg* [Br] 56:160–166.
- Layton MW, Goldstein SA, Goulet RW, Feldkamp LA, Kubinski DJ, Bole GG. 1988. Examination of subchondral bone architecture in experimental osteoarthritis by microscopic computed axial tomography. *Arthritis Rheum* 31:1400–1405.
- Macchiarelli R, Bondioli L, Galichon V, Tobias PV. 1999. Hip bone trabecular architecture shows uniquely distinctive locomotor behaviour in South African australopithecines. *J Hum Evol* 36:211–232.
- MacLatchy LM, Chen X. 1997. Comparison between external and internal bony architecture in the hominoid hip. *Am J Phys Anthropol* [Suppl] 24:159–160.
- MacLatchy L, Müller R. 2000. Trabecular architectural differences in primate proximal femora. *J Vert Paleontol* [Suppl] 3:55.
- Merz WA, Schenk RK. 1970. Quantitative structural analysis of human cancellous bone. *Acta Anat* 75:54–66.
- Mullender MG, Huiskes R, Versleyen H, Buma P. 1996. Osteocyte density and histomorphometric parameters in cancellous bone of the proximal femur in five mammalian species. *J Orthop Res* 14:972–979.
- Müller R, Koller B, Hildebrand T, Laib A, Gionollini S, Rügsegger P. 1996. Resolution dependency of microstructural properties of cancellous bone based on three-dimensional  $\mu\text{-tomography}$ . *Technol Health Care* 4:113–119.

- Müller R, Van Campenhout H, Van Damme B, Van der Perre G, Dequeker T, Hildebrand T, Rügsegger P. 1998. Morphometric analysis of human bone biopsies: a quantitative structural comparison of histological sections and micro-computed tomography. *Bone* 23:59–66.
- Odgaard A, Andersen K, Melsen F, Gundersen HJ. 1990. A direct method for fast three-dimensional serial reconstruction. *J Microsc* 159:335–342.
- Oxnard CE, Yang HC. 1981. Beyond biometrics: studies of complex biological patterns. *Symp Zool Soc Lond* 46:127–167.
- Parfitt AM, Mathews CHE, Villanueva AR, Kleerekoper M, Frame B, Rao DS. 1983. Relationships between surface, volume, and thickness of iliac trabecular bone in aging and osteoporosis. *J Clin Invest* 72:1396–1409.
- Pauwels F. 1960. *Biomechanics of the locomotor apparatus*. Berlin: Springer.
- Peyrin F, Houssard JP, Maurincomme E, Peix G, Goutte R, Laval-Jeantet AM, Amiel M. 1993. 3D display of high resolution vertebral structure images. *Comput Med Imag Graph* 17:251–256.
- Pope NS, Gould KG, Anderson DC, Mann DR. 1989. Effects of age and sex on bone density in the rhesus monkey. *Bone* 10:109–112.
- Radin EL, Parker HG, Pugh JW, Steingberg RS, Paul IL, Rose RM. 1973. Response of joints to impact loading—III: Relationship between trabecular microfractures and cartilage degeneration. *J Biomech* 6:51–57.
- Rafferty KL. 1996. Joint design in primates: external and subarticular properties in relation to body size and locomotor behavior. Dissertation. Baltimore: Johns Hopkins University.
- Rafferty KL. 1998. Structural design of the femoral neck in primates. *J Hum Evol* 34:361–384.
- Rafferty KL, Ruff CB. 1994. Articular structure and function in *Hylobates*, *Colobus*, and *Papio*. *Am J Phys Anthropol* 94:395–408.
- Rook L, Bondioli L, Köhler M, Moyà-Solà S, Macchiarelli R. 1999. *Oreopithecus* was bipedal ape after all: evidence from the iliac cancellous architecture. *Proc Natl Acad Sci USA* 96:8795–8799.
- Rowe T, Kappelman J, Carlson W, Ketcham R, Denison C. 1997. High resolution computed tomography: a breakthrough technology for earth scientists. *Geotimes* 42:23–27.
- Rügsegger P, Koller B, Müller R. 1996. A microtomographic system for the non-destructive evaluation of bone architecture. *Calcif Tissue Int* 58:24–29.
- Ryan TM. 2000. Quantitative analysis of trabecular bone structure in the femur of loroid primates using high resolution X-ray computed tomography. *Am J Phys Anthropol [Suppl]* 30:266–267.
- Ryan TM. 2001. The structure and function of trabecular bone in the femoral head of strepsirrhine primates. Dissertation. Austin: University of Texas at Austin.
- Simon SR, Radin EL. 1972. The response of joints to impact loading—II. In vivo behavior of subchondral bone. *J Biomech* 5:267–272.
- Spoor CF, Zonneveld FW, Macho GA. 1993. Linear measurements of cortical bone and dental enamel by computed tomography: applications and problems. *Am J Phys Anthropol* 91:469–484.
- Swartz SM, Parker A, Huo C. 1998. Theoretical and empirical scaling patterns and topological homology in bone trabeculae. *J Exp Biol* 201:573–590.
- Thomason JJ. 1985. The relationship of trabecular architecture to inferred loading patterns in the third metacarpals of the extinct equids *Merychippus* and *Mesohippus*. *Paleobiology* 11:323–335.
- Underwood EE. 1970. *Quantitative stereology*. Reading, MA: Addison-Wesley Publishing Co.